



Article

Demonstration of a Low-SWaP Terminal for Ground-to-Air Single-Mode Fiber Coupled Laser Links

Ayden McCann ^{*}, Alex Frost, Skevos Karpathakis, Benjamin Dix-Matthews, David Gozzard , Shane Walsh and Sascha Schediwy

International Centre for Radio Astronomy Research, The University of Western Australia, Perth 6009, Australia; alex.frost@research.uwa.edu.au (A.F.); skevos.karpathakis@research.uwa.edu.au (S.K.); benjamin.dix-matthews@uwa.edu.au (B.D.-M.); david.gozzard@uwa.edu.au (D.G.); shane.walsh@uwa.edu.au (S.W.); sascha.schediwy@uwa.edu.au (S.S.)

* Correspondence: ayden.mccann@research.uwa.edu.au

Abstract: Free space optical technology promises to revolutionize point-to-point communications systems. By taking advantage of their vastly higher frequencies, coherent optical systems outperform their radio counterparts by orders of magnitude in achievable data throughput, while simultaneously lowering the required size, weight, and power (SWaP), making them ideal for mobile applications. However, the widespread implementation of this technology has been largely hindered by the effects of atmospheric turbulence, often necessitating complex higher-order adaptive optics systems that are largely unsuitable for deployment on mobile platforms. By employing tip/tilt beam-stabilization, we present the results of a bespoke low-SWaP optical terminal that demonstrated single-mode fiber (SMF) coupling. This was achieved by autonomously acquiring and tracking the targets using a combination of aircraft transponder and machine vision feedback to a root-mean-square (RMS) tracking error of 29.4 μ rad and at angular rates of up to 0.83 deg/s. To the authors' knowledge, these works constitute the first published SMF coupled optical link to a full-sized helicopter, and we describe derived quantities relevant to the future refinement of such links. The ability to achieve SMF coupling without the constraints of complex adaptive optics systems positions this technology as a versatile quantum-capable communications solution for land-, air-, and sea-based platforms ranging across commercial, scientific, and military operators.



Citation: McCann, A.; Frost, A.; Karpathakis, S.; Dix-Matthews, B.; Gozzard, D.; Walsh, S.; Schediwy, S. Demonstration of a Low-SWaP

Terminal for Ground-to-Air Single-Mode Fiber Coupled Laser Links. *Photonics* **2024**, *11*, 633.

<https://doi.org/10.3390/photronics11070633>

Received: 6 June 2024

Revised: 27 June 2024

Accepted: 1 July 2024

Published: 2 July 2024



Copyright: © 2024 by the authors. Licensee MDPI, Basel, Switzerland. This article is an open access article distributed under the terms and conditions of the Creative Commons Attribution (CC BY) license (<https://creativecommons.org/licenses/by/4.0/>).

Keywords: acquisition and tracking; single-mode fiber; free space optical

1. Introduction

In the modern era, as the sheer amount of data generated increase, the demand for fast and efficient communications is inescapable. Wireless communications systems such as those found on aircraft, ships, terrestrial vehicles, and spacecraft are still largely dependent on radio technology and are struggling to keep up with this ever-increasing data demand [1–4].

The achievable data rate via wireless communication systems scales with the frequency of the carrier signal. Radio frequencies occupy the lowest section of the electromagnetic spectrum, making their use for high-speed communications sub-optimal [5,6]. In addition, data rates are also influenced by transmit power and receiver gain, meaning that the only way to increase the data rate of radio transmissions is to increase transmission power, transmitter or receiver size, or spectral efficiency. For mobile applications, increasing these parameters is especially problematic, as the size, weight, and power (SWaP) of a land, air, or sea-based vehicle is an extremely precious commodity. An increase in power usage, size, or weight significantly impacts the capabilities of a given system, or substantially adds to its cost. Due to these limitations, various systems face an on-board bottleneck, greatly limiting the capabilities of a system due to finite on-board data storage space [4].

Free-space optical (FSO) communications leverage the significantly higher frequencies used by modern fiber optic networks. This technology not only provides a substantial increase

in data rates but, through the high directionality of laser beams, offers benefits such as reduced SWaP requirements and significantly increased security. This makes it ideal for a host of civilian and military applications across land-, air-, sea-, and space-based vehicles. However, this high directionality places strict requirements on acquisition and tracking systems.

In addition, the simplest GSO communication schemes, known as direct detection, only require measuring the intensity of the received light. However, to take full advantage of the communication capacity of FSO and ensure compatibility with increasingly relevant quantum communication protocols, it is necessary to maintain phase and polarization information [7,8]. While direct detection methods can utilize comparatively large free-space detectors, phase and polarization coherence can only be achieved by coupling into a SMF with an 8–10 micron diameter. As a consequence, tracking requirements are further tightened, as precise alignment is crucial to ensure effective coupling into the narrow core of the SMF [9].

These coherent methods are also heavily affected by atmospheric turbulence [10,11]. Full adaptive optics (AO) systems, which include a wavefront sensor and deformable mirror to suppress higher-order effects, provide an effective way to combat these effects. Such AO systems have previously been used to achieve 100 Gbp/s bidirectional communications links between a fixed-wing aircraft and permanent optical ground station [12]. These AO systems, however, are costly, sensitive, and greatly increase the SWaP of a given system. This generally limits their suitability for deployment on portable or mobile platforms. Transportable ground-to-air systems have been also developed without these AO systems, but examples in the literature utilize direct-detection methods, limiting their data-carrying capacity rate and suitability for quantum communication [13,14].

In this paper, we present the results of an SMF coupled FSO retro-reflected link between a bespoke transportable optical terminal, deployed on a rooftop, and a helicopter at a folded link distance of ~ 10 km. Through the use of bespoke machine vision-based target identification and tracking software, the system achieves SMF coupling at angular velocities up to ~ 0.83 deg/s. This is achieved without the need for permanent ground station infrastructure or higher-order AO systems. In addition, to the authors' knowledge, this constitutes the first published optical link to a full-scale helicopter, and we describe derived quantities relevant to the future refinement of such links.

2. Methods

2.1. Ground Segment

2.1.1. Optical Terminal

The optical terminal used in this test is an evolution of the terminal described in Walsh et al. [15]. A simplified schematic of the terminal and supporting devices is shown in Figure 1. The system takes a fiber-fed laser input and collimates it to free space through the transmit collimator, FFC1. The beamsplitter, BS1, splits the beam. Half of the outgoing fiber power is directed to a beam trap, not shown, and half is directed to the lens L1. The beam is split once again by BS2, before being directed to an off-axis parabolic mirror, M1. L1 and M1 form a $15\times$ beam expander, resulting in an output beam waist diameter of 34 mm. This configuration is an upgrade on the terminal described in Walsh et al. [15], as the parabolic mirror and BS2 location prevent back reflections from the high-power laser input from entering, and saturating, the imaging arm. The tip/tilt (TT) mirror, M2, with an actuation range of 2 mrad, steers the output beam as it leaves the terminal.

For the tests described in this paper, a corner-cube retroreflector (CCR) in the airborne vehicle reflects the beam back into the terminal. On the return journey, half of the beam power is directed back towards L1 and into FFC2 to couple back into SMF for reception. In the configuration discussed in this paper, only 10% of the coupled power is directed to the avalanche photodiode for analysis. The remainder is channeled to an unrelated experiment, the results of which are outside of the scope of this work. The other half of the received power is directed towards the imaging arm via L2. L2 and M1 form a $7\times$ beam expander,

shrinking the beam diameter to approximately 7 mm. The return beam then passes to the short-wave infrared camera.

For target acquisition, the terminal features a commercial off-the-shelf (COTS) automatic dependent surveillance–broadcast (ADS-B) receiver in the form of a small antenna and software-defined radio. Additionally, the terminal incorporates a FLIR BlackFly S machine vision (MV) light camera fitted with a $f = 100$ mm lens to facilitate closed-loop target tracking. This configuration of the camera provides a wide $5^\circ \times 3.8^\circ$ field of view (FOV) and a $45 \mu\text{rad}$ pixel scale.

To assist in on-board payload acquisition, an additional beacon laser is coaligned with the primary beam and with a divergence of ~ 1 mrad. At 5 km, this equates to an approximately 5 m beam diameter. This largely encapsulates the fuselage of the helicopter used in these works, allowing for the detection of the CCR’s position on the aircraft, which is then targeted by the TT system, directing the narrower primary laser onto the optical payload.

For this demonstration, the terminal was installed on a COTS Planewave Instruments L-350 astronomical telescope mount to provide coarse pointing control; this is shown in Figure 2. The mount was then deployed onto the roof of the physics building at the University of Western Australia, as the location provides an uninterrupted line of sight to the majority of the sky, with the exception of a communications mast to the east.

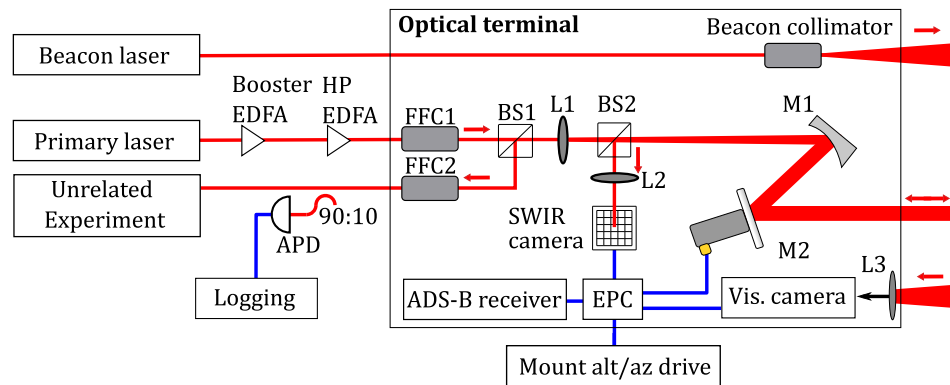


Figure 1. A schematic of the optical terminal used in the demonstration. Optical paths are depicted in red and electrical connections in blue. Key abbreviations include: APD—avalanche photodiode, alt/az—altitude/azimuth, BS—beamsplitter, EDFA—erbium-doped fiber amplifier, EPC—embedded computer, FFC—free-space-to-fiber collimator, HP—high power, L—lens, M—mirror, SWIR—short-wave infrared, and vis.—visible.

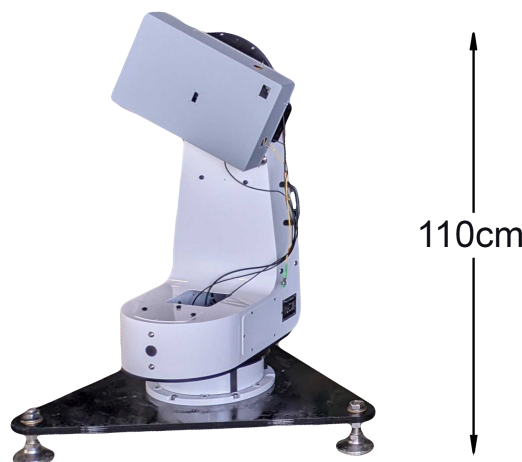


Figure 2. A photograph of the system used in the demonstrations described in this paper. The optical terminal is visible as a dark gray enclosure pointed diagonally. In this image, the telescope mount is affixed to a transportable steel base.

A best-case link budget for the demonstration is provided in Table 1. The link margin was reduced by dynamic factors during flight operations. An anticipated geometric loss of 23 dB was modeled and confirmed in a previous demonstration [16]. Additionally, the fiber coupling loss dynamically varies due to residual TT errors and atmospheric turbulence [12,17].

Table 1. Best-case link budget for the demonstration outlining the various sources of loss over the link.

Parameters	Value	
Transmitted fiber power	33	dBm
Geometric loss (10 km folded)	−23	dB
Terminal losses	−18	dB
Fiber coupling	−10	dB
Unrelated experiment	−10	dB
Received power	−28	dBm

2.1.2. Initial Acquisition

ADS-B transponders are present on most commercially operated fixed- and rotary-wing aircraft in Australia [18]. Our initial target acquisition technique leverages the broadcasts from these transponders through the use of our local receiver, which has been experimentally verified to receive ADS-B broadcasts from aircraft up to 213 km away. To acquire a target, the call sign of the aircraft is entered into our software graphical user interface (GUI), triggering a query of the list of currently tracked aircraft. If a match is found, the algorithm records the target's latest positional information (latitude, longitude, and altitude), as well as quantities regarding its current motion (heading, ground speed, and vertical rate). These parameters, as well as information detailing the age of the broadcast information, are used to generate new latitude, longitude, and altitude values by performing a linear extrapolation of the original position using the collected motion parameters. The pointing between the location of the terminal and the calculated target position is then transformed to altitude and azimuth coordinates sent to the mount to acquire the aircraft. The simple assumption of linear motion inevitably leads to angular error in the predicted pointing to the target. However, the large FOV of the subsequent MV target identification stage makes this error inconsequential in practical scenarios.

2.1.3. Target Identification and Tracking

To identify the target in the image of the visible light camera, a series of OpenCV MV algorithms are applied [19]. In order to smooth out contributions from noise and hot pixels, a 3×3 box-blur kernel is first applied to the image. Following this, an adaptive Gaussian thresholding algorithm is used. This algorithm identifies pixels that cross a threshold value determined by the Gaussian weighting of neighboring pixels. Given the varying brightness of the target aircraft and sky contributions, this more sophisticated algorithm provides vastly more robust target identification than the global thresholding used in our previous works [15]. For the parameters chosen in these tests (blockSize = 7, C = 10), the filtered images contain the outlines and hard internal edges of aircraft. These identified details are then dilated by a chosen number of pixels (set to 35 by default). Appropriate usage 'fills' the space between these pixels and recovers a singular object. This object can then be contoured, with the final target location in the image being regarded as the center of the minimum enclosing circle of this contour. The dilation stage can be as considered crucial in ensuring the process is robust against large gaps in the thresholding stage, producing several contours in varying brightness conditions. All parameters are easily adjusted in real time through the GUI.

These steps are demonstrated on an example aircraft in Figure 3. Due to the scarcity of hard-edged objects in the sky, this algorithm frequently performs as desired without additional filtering, and is robust against unwanted contributions from clouds. For more complex cases where images feature additional unrelated aircraft, or for low elevation targets that are in

close angular proximity to buildings and trees, a region of interest system can be engaged to filter the area under consideration in the image to remove their contributions during the target identification process. Due to the low computational requirements of this process, target identification can be performed at upwards of 30 Hz on the MV camera's 1936×1464 frames by the modest embedded computer utilized in these tests.

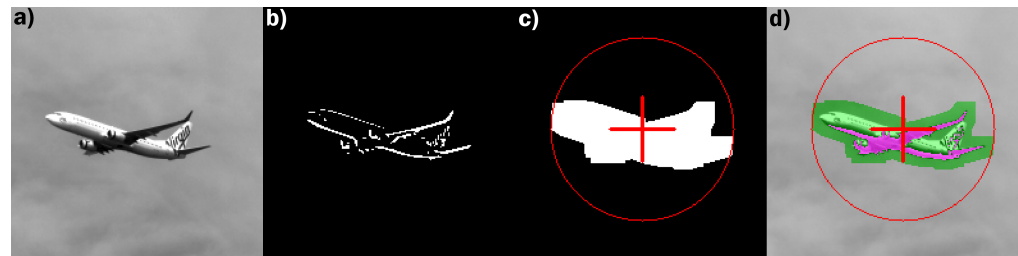


Figure 3. An example of the target identification algorithm during testing. (a) The original image. (b) Adaptive Gaussian thresholding. (c) Dilation algorithm and minimum enclosing circle. (d) The combined image displayed on the GUI. For brevity, the initial smoothing has been skipped as a panel in this graphic.

Then, using the camera's physical pixel size and focal length of the lens, the angular offset between the determined center of the targeted aircraft and the known position of the beacon laser is then input into a proportional, integral, derivative (PID) controller governing the corrective rates of the mount. Due to the dense air traffic in the Perth metropolitan region, the tuning of this PID controller is progressively optimized over the course of the project by tracking nearby aircraft (as evidenced by the commercial aircraft shown in Figure 3). Given the divergence of the beacon laser, a tracking accuracy of ≤ 1 mrad is required to ensure the beam is incident on the calculated center of the aircraft, with an increase in 0.2 mrad for every meter the optical payload is offset from this position at the nominal distance of 5 km. The operation of the aforementioned identification and tracking systems is controlled by our bespoke software GUI.

2.1.4. TT Adaptive Optics

As discussed in Frost et al. (in prep), given the predominantly non-TT wavefront perturbations associated with links of ~ 10 km, TT compensation does little to directly compensate for the impact of atmospheric turbulence, except at sufficiently low turbulence strengths [20]. However, given that the MV algorithm only identifies the center of the target aircraft, and that COTS astronomical telescope mounts are typically insufficient in robustly maintaining the accuracy required to place the returned power onto the receive collimator (FFC2 in Figure 1), the TT system is crucial in steering the beam accurately onto the on-board optical payload.

The beacon laser is used to locate the position of the payload. When illuminated, the CCR directs power back to the terminal, a portion of which is directed to the short-wave infrared camera. Due to its relative intensity when compared to the background, contributions returned from the CCR can be safely isolated by applying a simple global threshold on the received images and then calculating the weighted center of the remaining pixels. This is converted to an angular difference between the current pointing and the predetermined location of the primary laser and input into an additional PID controller operating at 100 Hz governing control of the TT mirror, M2.

2.2. Air Segment

2.2.1. Optical Payload

The onboard payload consisted of a 2.5-inch CCR mounted on a tripod, with a viewfinder scope to facilitate manual alignment with the ground segment (Figure 4a). During the test, the payload was affixed to the floor directly in front of the open main door on the right-hand side of the aircraft. This corresponds to being almost directly underneath the center of the helicopter's main rotor.

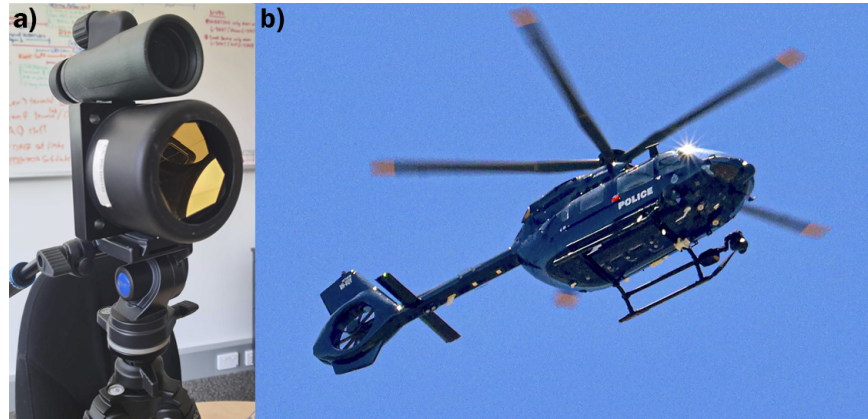


Figure 4. (a) CCR-based optical payload carried on board the helicopter. (b) The Airbus H145 helicopter used during the optical link demonstration.

2.2.2. Flight Dynamics

The aircraft utilized for the demonstration was an Airbus H145 helicopter operated by the Western Australian Police Force Air Wing (Figure 4b). The helicopter initially departed from Jandakot Airport approximately 15 km south east of the terminal before climbing to an altitude of 3 km to commence the demonstration phase of the flight. This phase spanned approximately 20 min and consisted of two circular orbits at a line-of-sight distance of 4.9–5.6 km. This included a 7 min period of hovering part-way through the first orbit, as shown in Figure 5. Data were collected for both orbits, with the hovering portion of the flight dedicated to communicating to the crew via radio and consolidating captured data.

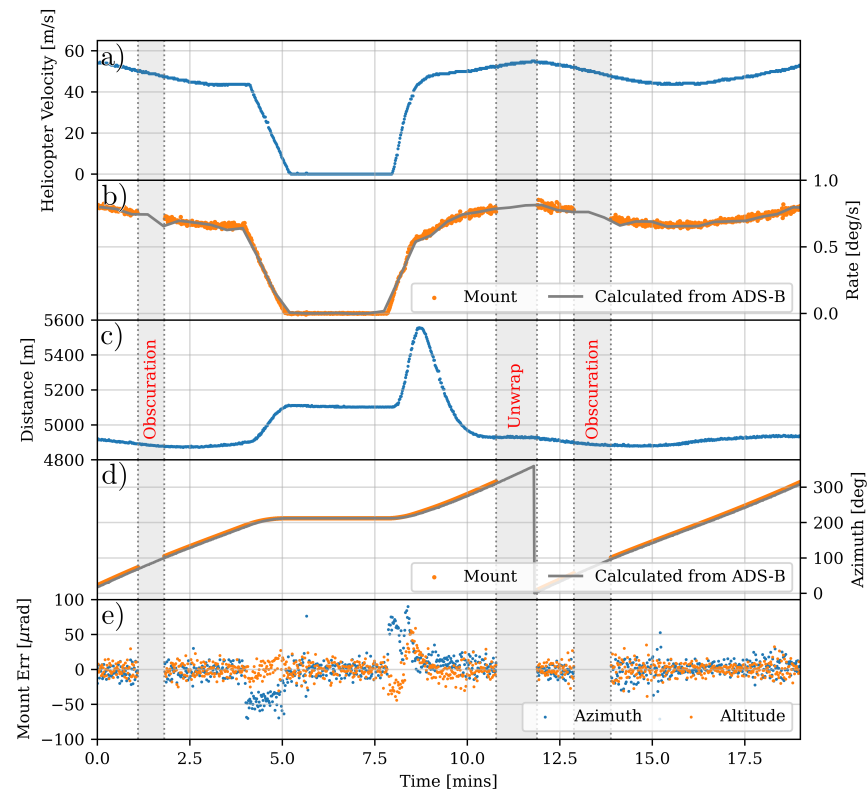


Figure 5. Spatial time series data from the demonstration. (a) Aircraft velocity from ADS-B data. (b) ADS-B and mount angular rate determinations. (c) Distance between the terminal and the helicopter. (d) Azimuth position, demonstrating the periods of circular motion and hovering. (e) Mount tracking error. Given error during acquisition begins orders of magnitude larger than the prolonged tracking error; initial convergence has been omitted for enhanced clarity.

Previous demonstrations have indicated the presence of micron-sized particles, which act to impose apparent losses through the process of Mie scattering [11,15]. However, publicly available data indicate that conditions on the day of the demonstration were favorable for the optical link, with a median PM_{2.5} density of 1.4 µg/m³, typical of the demonstration area.

3. Results and Discussion

3.1. Acquisition and Tracking

Positions extrapolated from the ADS-B receiver were consistent in placing the target in the FOV of the MV. The high elevation of the targets provided frequent ADS-B broadcasts to the local receiver and, given the nominal line-of-sight distance of 5 km between the terminal and the target, residual errors from linear extrapolation constituted a small fraction of the total FOV.

The MV target identification system was successful in determining the aircraft location within each frame and providing angular error information for mount corrections. However, individual pixels close to the threshold of the adaptive thresholding algorithm, exacerbated by the dilation procedure, created high-frequency noise in the determined target location (visible in the bottom panel of Figure 5). In order to prevent this noise from invoking rapid erroneous corrective movements and putting pressure on the TT system, the PID controller governing the motion of the mount was ‘detuned’ with a low proportional term and high integral term ($P = 1.9$, $D = 4$, $I = 0.3$). This was at the expense of response to rapid acceleration. An increase in mount error is seen at 4.5 and 8 min in Figure 5 where this occurred pre- and post-hover phase. However, these increases equated to ~5% of the 2 mrad TT actuation range, making the detuned tracking more than adequate in maintaining the required accuracy once the TT system was locked.

After initial convergence, the observed pre-TT root-mean-square (RMS) tracking error of the system was 29.4 µrad at a maximum angular rate of 0.83 deg/s. Given this is drastically lower than the ≈ 1 mrad error required to illuminate the optical payload with the beacon laser, reliable identification of the optical payload by the TT system link was achieved. This allowed for rapid re-acquisition of the link after the interruptions caused by the required unwrap of the mount (visible at ~11.5 min in Figure 5) and occlusion by the nearby communications mast (visible at ~1.5 and 13.5 min in Figure 5).

3.2. Optical Link

To assess the quality of the coupling into SMF, the data collected by the avalanche photodiode during the uninterrupted segment of the flight following the second obscuration were utilized. The scintillation index was defined as:

$$SI = \frac{\sigma_{P_{rx}}^2}{\mu_{P_{rx}}^2} \quad (1)$$

where $\sigma_{P_{rx}}$ and $\mu_{P_{rx}}$ are the standard deviation and mean of received power, P_{rx} , respectively. Coherence time was defined as the time duration where the normalized auto-correlation of the measured power dropped below $1/e$.

The scintillation index calculated during the flight was 3.85. This is considerably higher than previous results over a stationary link of similar distance [16]. This information, coupled with the derived coherence time of 7.92 ms and the presence of the spike contribution at approximately 600 Hz shown in the normalized received power spectral density presented in Figure 6, suggests that the primary source of link degradation was downwash from the main rotor of the helicopter, which would have produced significant turbulence in the direct vicinity of the optical payload, vibration incident on the optical payload, or, more likely, a combination of the two.

Figure 7 displays histograms of received power normalized to mean (a) and probability of fade (b). These results demonstrate a high level of fiber coupling loss, again suggesting strain due to the aforementioned air segment dynamics. From the data, to attain a probability of fade at 10^{-4} , a power margin of 26.8 dB is required.

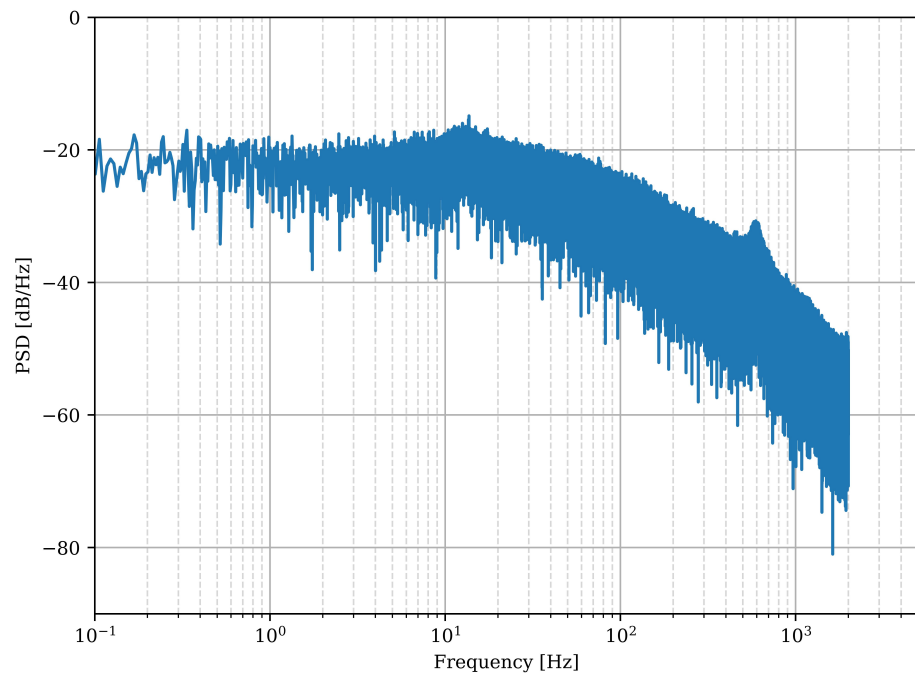


Figure 6. The normalized spectral density of the received SMF power over the helicopter demonstration. A spike in frequency contribution is visible at approximately 600 Hz, suggesting the dynamics specific to the helicopter have caused appreciable degradation to the stability of the coupled fiber power.

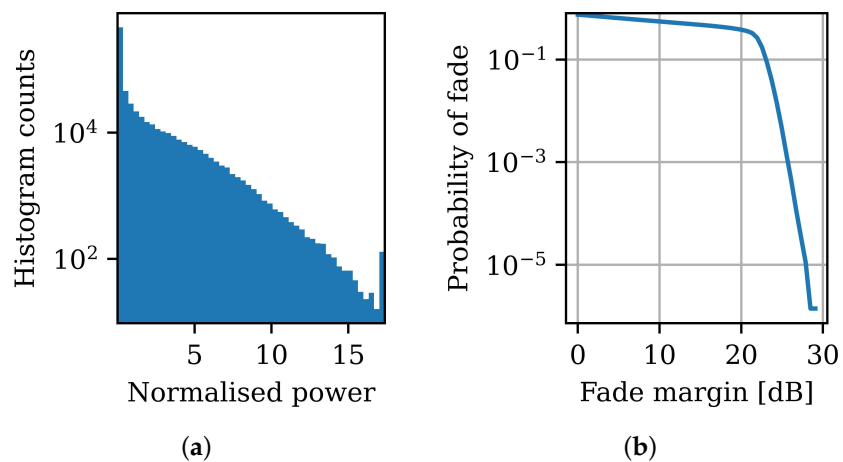


Figure 7. Channel characteristics of the received SMF power by the avalanche photodiode following the second obscuration visible in Figure 5. (a) Power received. (b) Probability of fade. Both plots indicate the severe and frequent presence of turbulence-induced fading, with (b) suggesting that, to ensure link stability, greater transmit power is required in the absence of higher-order AO systems.

4. Conclusions

We have demonstrated the ability of our system to acquire and track aircraft to the levels of accuracy required to facilitate SMF coupled optical links to aircraft with pre-TT RMS pointing errors of 29.4 μ rad, at angular rates of up to 0.83 deg/s. These results affirm the suitability of low SWaP iterations of this technology for further development and testing across land, air, and sea environments for both scientific and communications applications.

Analysis of the SMF channel characteristics demonstrated a highly turbulent link, and the observed coherence time of 7.92 ms and high frequency contributions of the analyzed power spectrum suggest this volatility was due to the unique turbulence conditions presented by the helicopter. Results show that in TT-only systems the observed dynamical

losses require a significant power margin in order to produce links with consistent power, and this information will be utilized in future generations of the optical terminal.

Future work can disentangle the contributions of rotor downwash and transverse air due to movement in future helicopter-based links by repeating the test with adequate data from the helicopter in a hovering position. The implementation of a true airborne terminal capable of autonomous acquisition and tracking similar to that described for the ground segment would shed light on dynamics specific to the impact of the alignment and vibration of the air segment.

Author Contributions: A.M. wrote the manuscript with input from all authors, developed the target acquisition, tracking, and TT systems, and conducted all data analysis and interpretation included. A.F. and B.D.-M. designed and assembled optics. S.K. assisted data analysis. S.S built and operated the optical payload during the fixed-wing test. D.G., S.W. and S.S. conceived the experiment. All authors have read and agreed to the published version of the manuscript.

Funding: This work has been supported by the SmartSat CRC, whose activities are funded by the Australian Government’s CRC Program. A.M. and A.F. are supported by Australian Government Research Training Program Scholarships and top-up scholarships funded by the Government of Western Australia. S.K. is supported by a SmartSat CRC PhD Scholarship.

Data Availability Statement: The datasets used and/or analyzed during the current study available from the corresponding author on reasonable request.

Acknowledgments: The authors wish to thank the Western Australian Police Force Air Wing for providing the aircraft utilized during these works, as well as Colby Gaynes for granting permission to use his photograph of the aforementioned aircraft in Figure 4.

Conflicts of Interest: The authors declare no conflicts of interest.

Abbreviations

The following abbreviations are used in this manuscript:

ADS-B	automatic dependent surveillance–broadcast
AO	adaptive optics
APD	avalanche photodiode
CCR	corner-cube retroreflector
COTS	commercial off-the-shelf
EM	electromagnetic
FOV	field of view
FSO	Free-space optical
GUI	graphical user interface
MV	machine vision
PID	proportional, integral, derivative
PSD	power spectral density
RMS	root-mean-square
SMF	single-mode fiber
SWaP	size, weight, and power
SWIR	short-wave infrared
TT	tip/tilt
UWA	University of Western Australia.

References

1. Horyna, J.; Walter, V.; Saska, M. UVDAR-COM: UV-based relative localization of UAVs with integrated optical communication. In Proceedings of the 2022 International Conference on Unmanned Aircraft Systems (ICUAS), Dubrovnik, Croatia, 21–24 June 2022; IEEE: Piscataway, NJ, USA, 2022; pp. 1302–1308.
2. Yang, T.; Li, J.; Feng, H.; Cheng, N.; Guan, W. A Novel Transmission Scheduling Based on Deep Reinforcement Learning in Software-Defined Maritime Communication Networks. *IEEE Trans. Cogn. Commun. Netw.* **2019**, *5*, 1155–1166. [[CrossRef](#)]
3. Rehmus, P.; Congress of the United States, Congressional Budget Office. *The Armys Bandwidth Bottleneck*; Congress of the United States, Congressional Budget Office: Washington, DC, USA, 2003.

4. Davidson, R.; Bridges, C.P. Adaptive multispectral GPU accelerated architecture for Earth Observation satellites. In Proceedings of the 2016 IEEE International Conference on Imaging Systems and Techniques (IST), Chania, Greece, 4–6 October 2016; IEEE: Piscataway, NJ, USA, 2016; pp. 117–122.
5. Shannon, C.E. A mathematical theory of communication. *Bell Syst. Tech. J.* **1948**, *27*, 379–423. [[CrossRef](#)]
6. Ghatak, A.K. Fibre Optics and Optical Communications: A Perspective. *Iete Tech. Rev.* **1990**, *7*, 229–246. [[CrossRef](#)]
7. Ip, E.; Lau, A.P.T.; Barros, D.J.; Kahn, J.M. Coherent detection in optical fiber systems. *Opt. Express* **2008**, *16*, 753–791. [[CrossRef](#)] [[PubMed](#)]
8. Sisodia, M.; Omshankar; Venkataraman, V.; Ghosh, J. FSO-QKD protocols under free-space losses and device imperfections: A comparative study. *Quantum Inf. Process.* **2024**, *23*, 185. [[CrossRef](#)]
9. Kaymak, Y.; Rojas-Cessa, R.; Feng, J.; Ansari, N.; Zhou, M.; Zhang, T. A survey on acquisition, tracking, and pointing mechanisms for mobile free-space optical communications. *IEEE Commun. Surv. Tutor.* **2018**, *20*, 1104–1123. [[CrossRef](#)]
10. Strohbehn, J.W. Line-of-sight wave propagation through the turbulent atmosphere. *Proc. IEEE* **1968**, *56*, 1301–1318. [[CrossRef](#)]
11. Ricklin, J.C.; Hammel, S.M.; Eaton, F.D.; Lachinova, S.L. Atmospheric channel effects on free-space laser communication. *J. Opt. Fiber Commun. Rep.* **2006**, *3*, 111–158. [[CrossRef](#)]
12. Chen, C.; Grier, A.; Malfa, M.; Booen, E.; Harding, H.; Xia, C.; Hunwardsen, M.; Demers, J.; Kudinov, K.; Mak, G.; et al. Demonstration of a bidirectional coherent air-to-ground optical link. In Proceedings of the Free-Space Laser Communication and Atmospheric Propagation XXX, San Francisco, CA, USA, 29–30 January 2018; SPIE: St Bellingham, WA, USA, 2018; Volume 10524, pp. 120–134.
13. Moll, F.; Horwath, J.; Shrestha, A.; Brechtelsbauer, M.; Fuchs, C.; Navajas, L.A.M.; Souto, A.M.L.; Gonzalez, D.D. Demonstration of high-rate laser communications from a fast airborne platform. *IEEE J. Sel. Areas Commun.* **2015**, *33*, 1985–1995. [[CrossRef](#)]
14. Walther, F.G.; Michael, S.; Parenti, R.R.; Taylor, J.A. Air-to-ground lasercom system demonstration design overview and results summary. In *Proceedings of the Free-Space Laser Communications X*; SPIE: San Diego, CA, USA, 2010; Volume 7814, pp. 256–264.
15. Walsh, S.M.; Karpathakis, S.F.; McCann, A.S.; Dix-Matthews, B.P.; Frost, A.M.; Gozzard, D.R.; Gravestock, C.T.; Schediwy, S.W. Demonstration of 100 Gbps coherent free-space optical communications at LEO tracking rates. *Sci. Rep.* **2022**, *12*, 18345. [[CrossRef](#)] [[PubMed](#)]
16. Karpathakis, S.F.; Dix-Matthews, B.P.; Gozzard, D.R.; Schediwy, S.W. High-bandwidth coherent optical communication over 10.3 km of turbulent air. *Appl. Opt.* **2023**, *62*, G85–G89. [[CrossRef](#)] [[PubMed](#)]
17. Trinh, P.V.; Carrasco-Casado, A.; Okura, T.; Tsuji, H.; Kolev, D.R.; Shiratama, K.; Munemasa, Y.; Toyoshima, M. Experimental channel statistics of drone-to-ground retro-reflected FSO links with fine-tracking systems. *IEEE Access* **2021**, *9*, 137148–137164. [[CrossRef](#)]
18. Civil Aviation Safety Authority. Part 91 Manual of Standards: Division 26.16 ‘Surveillance Equipment’. Available online: <https://www.casa.gov.au/part-91-manual-standards> (accessed on 19 October 2023)
19. Bradski, G. The opencv library. In *Dr. Dobb’s Journal: Software Tools for the Professional Programmer*; OpenCV team: Palo Alto, CA, USA, 2000; Volume 25, pp. 120–123.
20. Frost, A.; Dix-Matthews, B.P.; Walsh, S.M.; Gozzard, D.R.; Schediwy, S.W. Optimal Design of Small Aperture Optical Terminals for Free-Space Links. Centre for Radio Astronomy Research, The University of Western Australia, Perth, Australia. 2024, *in preparation*.

Disclaimer/Publisher’s Note: The statements, opinions and data contained in all publications are solely those of the individual author(s) and contributor(s) and not of MDPI and/or the editor(s). MDPI and/or the editor(s) disclaim responsibility for any injury to people or property resulting from any ideas, methods, instructions or products referred to in the content.